Towards Lattice-Boltzmann modelling of unconfined gas mixing in anaerobic digestion

Davide Dapelo [a,*], Robin Trunk [b], Mathias J. Krause [b], John Bridgeman [a]

[a] Faculty of Engineering and Informatics, University of Bradford, Bradford, BD7 1DP, United Kingdom
[b] Lattice Boltzmann Research Group, Karlsruhe Institute of Technology, Karlsruhe, Germany

ARTICLE INFO

ABSTRACT

A novel Lattice-Boltzmann model to simulate gas mixing in anaerobic digestion is developed and described. For the first time, Euler–Lagrange multiphase, non-Newtonian and turbulence modelling are applied jontly with a novel hybrid boundary condition. The model is validated in a laboratory-scale framework and flow patterns are assessed through Particle Imaging Velocimetry (PIV) and innovative Positron-Emission Particle Tracking (PEPT). The model is shown to reproduce the experimental flow patterns with fidelity in both qualitative and quantitative terms.

The model opens up a new approach to computational modelling of the complex multiphase flow in anaerobic digesters and offers specific advantages, such as computational efficiency, over an analogous Euler-Lagrange finite-volume computational fluid dynamics approach.

1. Introduction

Wastewater treatment is an energy-intensive process. According to EU figures, the annual energy consumption of wastewater treatment works (WwTWs)'s in Member States exceeds 23,800 GWh [8], and an increase of 60% in the next 10–15 years is expected, principally due to tightened regulation of effluent discharges from WwTWs (e.g. Water Framework Directive, WFD) [14]. At the same time, the global need for water is expected to grow by 30%, and food and energy by 50% in the forthcoming decades [45]. From the perspective of climate change, this constitutes a "perfect storm", which makes it necessary to address the link between water and energy.

Municipal sewage sludge is the by-product of wastewater industry, with 1.5M tonnes produced annually in the UK [42]. Sludge is usually treated via anaerobic digestion, in which it is mixed with anaerobic bacteria at 22–41 °C. Mixing, in UK WwTWs is usually effected via gas mixing, in which a proportion of the produced biogas is collected and pumped back inside the digester and injected into the sludge via a series of nozzles. As bacteria degrade sludge to more stable compounds, a methane-rich biogas is produced. This can be harnessed as a renewable energy source, usually through combined heat and power technology. Mixing is crucial for stable process operation and accounts for a large portion

of a digester's energy consumption (17–73%, Owen [29]). However current practice in digester design is still rooted in rules of thumb and empiricism rather than science [10]. It is therefore clear that mixing design and operation should be optimised to achieve a better balance between input mixing energy and output biogas yield. Kress et al. [21] shown experimentally that it is possible to halve input mixing energy without impacting nutrient distribution, and hence, without impacting biogas yield.

Sludge is corrosive, biochemically hazardous and opaque; this makes the task of performing experiments on it challenging. Moreover, industrial digesters often consist of large tanks ($\sim$ 500 m^3) operating without interruptions. Under these conditions, the only feasible experimental option consists of injecting a tracer, usually lithium, to develop a tracer response curve, but still is a costly technique, which only provides a "black-box" representation of the flow patterns inside a digester. For this reason, numerical modelling has a major role to play to assist our understanding of mixing in anaerobic digestion.

Sludge is a complex, multiphase non-Newtonian fluid [13], and any numerical model aimed at modelling flow patterns inside an anaerobic digester must include sludge's relevant rheological characteristics. Considering the above-mentioned difficulties in accessing operational data, a common approach consists of providing a validation for the numerical model through laboratory-scale experiments, and then, applying the validated model to a full-scale case [11,12].

* Corresponding author.
  E-mail address: ddapelo@bradford.ac.uk (D. Dapelo).

Nomenclature

ε_K	Smoothing parameter of the K-th particle
$\dot{\gamma}$	Shear rate, s^{-1}
τ_K	Hydrodynamics torque acting on the K-th particle
μ	Power-law apparent viscosity, Pa s
$\mu_{\max}$	Power-law apparent maximum viscosity, Pas
$\mu_{\min}$	Power-law apparent minimum viscosity, Pas
ν	Dimensionless kinematic viscosity (before Smagorinsky correction)
ξ	Partial-slip parameter
ν_{eff}	Turbulent dimensionless kinematic viscosity
ρ^{C}	Continuous phase dimensionless density
ρ^{P}	Particulate phase dimensionless density
τ	Dimensionless relaxation time (before Smagorinsky correction)
τ_{eff}	Turbulent dimensionless relaxation time
$\boldsymbol{\Omega}_K$	Angular velocity of the K-th particle
$\boldsymbol{\alpha}_K$	Angular acceleration of the K-th particle
ϑ_K	Angular coordinate of the K-th particle
$\mathbf{a}_K$	Centre-of-mass acceleration of the K-th particle
C_{Smago}	Smagorinsky constant
$\mathbf{c}_i$	i-th discretized lattice velocity
c_s	Speed of sound
d	Porosity
$\mathbf{F}_K$	Hydrodynamics force acting on the K-th particle
f_i	i-th particle distribution function
$f_i^{\star}$	i-th particle distribution function after collision
$f_i^{(1)}$	i-th non-equilibrium particle distribution function
$f_i^{(\text{eq})}$	i-th equilibrium particle distribution function
g_i	Momentum exchange between two contiguous nodes across the i-th lattice direction
J_K	Moment of inertia of the K-th particle
K	Power-law consistency coefficient, Pa s^n
M_K	Mass of the K-th particle
n	Power-law index
N	Number of lattice nodes across the diameter
$\mathscr{P}_K$	K-th particle
q	Air injection flow rate for the experimental rig, ml s^{-1}
R_K	Radius of the K-th particle
$\mathbf{S}$	Rate of shear tensor
t	Dimensionless discretized time
$\mathbf{u}$	Dimensionless velocity
$\mathbf{U}_K$	Centre-of-mass velocity of the K-th particle
$\mathbf{u}^{\text{C}}$	Continuous phase dimensionless velocity
$\mathbf{u}^{\text{P}}$	Particulate phase dimensionless velocity
w_i	Weight of the i-th component of the equilibrium particle distribution
$\mathbf{x}$	Dimensionless lattice site coordinate
$\mathbf{x}_{\text{B}}$	Dimensionless lattice site coordinate at a partial-slip boundary node
$\mathbf{X}_K$	Centre-of-mass coordinate of the K-th particle
BGK	Bhatnagar–Gross–Krook
HLBM	Homogenised Lattice-Boltzmann method
LBM	Lattice-Boltzmann method
PEPT	Positron emission particle tracking
PIV	Particle image velocimetry
TS	Total solid content
WFD	European union's water framework directive
WwTW	Wastewater treatment work

A considerable amount of numerical work has been performed in the last decades for anaerobic digestion [7,9,10,12,17,18,26–28,33,38,41,43,46]. Despite the considerable advances in the understanding of mixing in anaerobic digestion, many important aspects still need to be clarified: research on mechanical mixing is exceeds gas mixing, and the link between mixing and biogas yield has not been thoroughly investigated.

To date, all the numerical work in anaerobic digestion has been limited to computational fluid dynamics (CFD) only. More recently, an alternative approach, the Lattice-Boltzmann (LB) method, has been developed. Lattice-Boltzmann presents determinant advantages over CFD, such as: (*i*) a simple updating algorithm free from resource-consuming loops otherwise necessary to solve the Navier–Stokes/pressure equations implicitly; (*ii*) a highly-parallelizable approach due to the locality of the processes; and (*iii*) a structure which allows the relatively simple and organic description of a variety of phenomena. These advantages ensure an unparalleled level of numerical efficiency: for instance, Lattice-Boltzmann can take advantage form modern massively parallel hardware like GPUs [19]. Hence, there is an obvious interest and benefit to be derived from developing Lattice-Boltzmann models for anaerobic digestion.

The aim of the work reported in this paper is to demonstrate the first step towards the simulation of flow patterns inside an anaerobic digester using the Lattice-Boltzmann framework and, in particular, the first-ever LB model for anaerobic digestion is described and subsequently validated against experimental laboratory data. The highly innovative model involves the combined application of a recent Euler–Lagrangian model, the Homogenised Lattice-Boltzmann Model (HLBM, Krause et al. [20] and Trunk et al. [39]) and a non-Newtonian model for the liquid phase [6] with an associated Smagorinsky turbulence closure model [15], and the introduction of a hybrid bounce-back/free-slip boundary condition.

This paper is structured as follows. First, sludge rheology and characteristics are summarized, and assumptions and modelling choices are discussed. The experimental apparatus and the visual imaging techniques adopted to produce the experimental data are then described. A discussion of the results follows, and conclusions drawn.

2. Materials and methods

2.1. Modelling assumptions

Sludge is a complex mixture of water, organic and inorganic matter. This complexity is further enhanced in digesters via the injection of biogas bubbles. The dimensions of the solid debris vary from molecules to sand and grit of approximately one millimetre, and possibly to centimetres if silage or food waste are added as in the case of agricultural digesters. The co-existence of liquid, solid and gas phases gives rise to a number of multiphase phenomena such as liquid-bubble momentum exchange, sedimentation and flotation. The presence of a bubbly phase due to biogas mixing gives rise to multiphase phenomena such as liquid-bubble momentum transfer and possibly bubble coalescence and breakup, and alterations at the liquid phase's surface. The presence of a solid phase alters the liquid phase rheology depending on the total solids content (TS) and the temperature [1], and gives rise to a wide series of non-Newtonian phenomena such as shear thinning and thixotropy [13]. Finally, the anaerobic digestion process means that bacteria break down complex molecules into smaller compounds as a result of their metabolic activities, and as a consequence, sludge's rheological characteristics may change throughout digestion progress [16].

Considering the complexity of the above-described phenomena, in order to model sludge successfully, it is necessary to introduce a series of assumptions as listed below.

Table 1
Rheological properties of sludge at $T = 35$ °C. From Laundry et al. [25].

TS (%)	K (Pa s^n)	n (–)	$|\dot{\gamma}|$ range (s^{-1})	$\mu_{\min}$ (Pa s)	$\mu_{\max}$ (Pa s)	Density (kg m^{-3})
2.5	0.042	0.710	226−702	0.006	0.008	1,000.36
5.4	0.192	0.562	50−702	0.01	0.03	1,000.78
7.5	0.525	0.533	11−399	0.03	0.17	1,001.00
9.1	1.052	0.467	11−156	0.07	0.29	1,001.31
12.1	5.885	0.367	3−149	0.25	2.93	1,001.73

2.1.1. Liquid phase

Sedimentation and flocculation take place through on scale of days if not years. The model illustrated in this work was developed from the perspective of improving the day-to-day balance between the degree of mixing and input mixing energy for a full-scale digester. Common mixing operation in WwTWs is broken down in cycles of one hour, and Dapelo and Bridgeman [11] shown that such a balance could be traced in around 15 min operational time. For this reason, the liquid and solid phases were modelled together as a single liquid phase, and sedimentation and flocculation were ignored.

2.1.2. Rheology

Non-Newtonian behaviour has been shown to alter the sludge flow patterns inside a digester [44], and consequently an effective model for mixing in anaerobic digestion should include non-Newtonian behaviour. A simple and robust model is the pseudoplastic model in which apparent viscosity μ and shear rate $\dot{\gamma}$ obey a power-law relationship:

$$\mu = K\dot{\gamma}^{n-1} , \tag{1}$$

where "pseudoplastic" means $n < 1$, and K is the consistency coefficient. In order to avoid non-physical divergence at zero shear rate or exceedingly low apparent viscosity values at high shear rates, the model defines a minimum and a maximum boundary for the apparent viscosity, namely $\mu_{\min}$ and $\mu_{\max}$ respectively. Landry et al. [25] performed a series of rheological measurements for sludge at different TS values, and the results are reported in Table 1.

The data show that the difference in density of sludge compared to that of water at 35 °C (994 kg m^{-3}) less than 1%. Therefore, for the sake of simplicity, sludge density was set to 1,000 kg m^{-3} for all simulations. Thyxotropy and dependence on digestion process were ignored because of the continuous nature of mixing and the short timescale involved (< 1 h in the experiment, against 15–30 days in full-scale operation).

2.1.3. Bubbly phase and multiphase model

Mixing is driven by the rise of a bubble plume. Hence, in order to obtain a faithful simulation of the flow patterns throughout the computational domain, a robust modelling of the bubble-liquid phase momentum exchange is required. However, a detailed description of the bubble dynamics is unimportant. Moreover, as shown in Section 2.3, no bubble breakup or coalescence is reported for the experimental apparatus taken in consideration. For full-scale plants, an experimental description of the bubble dynamics is unavailable due to the afore-mentioned black-box nature of the experimental techniques. However, Dapelo and Bridgeman [12] shown that a change in bubble size produced only marginal effects in the simulated flow patterns and no alteration in the quality of mixing.

An Euler–Lagrange modelling approach was considered as more suitable here than an Euler–Euler approach because it would require comparably less empirical information to close the equations of motion [2]. Considering the above factors, a two-way coupling (i.e. bubbles exchange momentum with liquid phase and vice versa) was adopted, and bubbles were modelled as rigid spheres.

The choice of an Euler–Lagrange model means that the evolution of the interface surface, and notably the top liquid-atmosphere surface, cannot be simulated directly. However, the bubble plume is expected to alter the surface by inducing a bulge at the top of the plume, and ripples departing from it, as reported in Section 2.3.2. Such displacements are expected to subtract energy from the bulk flow by turning it into potential energy (production of a bulge above the surface), and kinetic energy (surface waves and displacement of the atmosphere above). Since the effect of this dissipation phenomenon to the bulk flow could not be simulated directly, an attempt to reproduce this mechanism was performed by introducing a partial-slip boundary condition at the surface, in place of the free-slip. This was expected to subtract a portion of momentum from surface flow through dissipation and avoid it to be returned into the bulk flow.

2.2. Numerical model

The modelling assumptions discussed in Section 2.1.3 dovetail with the HLBM [20,39]. Compared to mainstream two-phase models such as the Shan–Chen [32] and the free energy,[36,37], the HLBM has the advantage of being free from pressure fluctuations and parasite interface flows and to naturally allow high phase density ratios ($\sim 10^3$) with no algorithm adaptation. Compared to immersed methods [30,40], it has the advantage of not needing mesh adaptation procedures.

2.2.1. The Lattice-Boltzmann framework

The Lattice-Boltzmann is a mesoscopic model. Unlike CFD and other macroscopic models, where the observable fields of velocity, density and pressure are solved directly, in Lattice-Boltzmann the fundamental object of interest is the one-particle density function $f(\mathbf{x}, \mathbf{c}, t)$, which describes the probability of finding a particle of fluid within the elemental cube $(\mathbf{x}, \mathbf{x} + d\mathbf{x})$ with a velocity comprised within the cubic interval $(\mathbf{c}, \mathbf{c} + d\mathbf{c})$ at a time t. Density $\rho(\mathbf{x}, t)$, velocity $\mathbf{u}(\mathbf{x}, t)$ and shear stress $\sigma(\mathbf{x}, t)$ are obtained from the zeroth, first and second moments of f [22]:

$$\rho = \int f \, d\mathbf{c} ; \tag{2}$$

$$\rho \mathbf{u} = \int f \mathbf{c} \, d\mathbf{c} ; \tag{3}$$

$$\rho \mathbf{u} \otimes \mathbf{u} - \sigma = \int f \mathbf{c} \otimes \mathbf{c} \, d\mathbf{c} . \tag{4}$$

The particle-density function obeys the Boltzmann equation:

$$(\partial_t + \mathbf{c} \cdot \nabla)f = \mathscr{C}(f) , \tag{5}$$

where $\mathscr{C}(f)$ is the collision operator, which models the effect of binary particle collisions. Eq. (5) can be considerably simplified following the Bhatnagar–Gross–Krook (BGK) collision operator [4], which hypothesised that the effect of a collision on f can be modelled as an exponential relaxation towards the equilibrium particle density function $f^{(\mathrm{eq})}$:

$$\mathscr{C}(f) = -\frac{1}{\tau}\big[f - f^{(\mathrm{eq})}\big] , \tag{6}$$

where τ is the relaxation time, and $f^{(\mathrm{eq})}$ is the Maxwell equilibrium distribution [22].

Discretization is performed as follows. The three-dimensional vectorial space describing the spatial coordinate is substituted with a cubic lattice with lattice size δx. The three-dimensional vectorial space describing the velocities is substituted with a finite and isotropic set of velocities pointing to the zeroth, first, second and

third neighbour of a given lattice site, with modulus respectively $\sqrt{0}$, $\sqrt{1}$, $\sqrt{2}$ and $\sqrt{3}$ times $\delta x/\delta t$, where δt is the timestep. Every discretization is conventionally identified by a tag DdQp, with d the dimensionality of the problem, and p the number of lattice velocities. Notationally, the continuous $f(\mathbf{x}, \mathbf{c}, t)$ is re-written as a set $f_i(\mathbf{x}, t)$, $i = 0, \ldots, p$, each defined at the lattice sites and referring to a discrete velocity $\mathbf{c}_i$. The integrals in Eqs. (2)–(4) are substituted with summations over the velocity set. The error arising from the discretization of the velocity set is cancelled by writing the Maxwell equilibrium function in terms of orthonormal Hermite polynomials. To recover the adiabatic dynamics with a compressibility error of Ma^2 with Ma being the Mach number, only the zeroth, first and second-order Hermite polynomials for the equilibrium function are necessary. In this way, $f^{(eq)}$ is written as:

$$f_i^{(eq)} = w_i \rho \left[1 + \frac{\mathbf{u} \cdot \mathbf{c}_i}{c_s^2} + \frac{(\mathbf{u} \cdot \mathbf{c}_i)^2 - c_s^2 u^2}{2c_s^4} \right], \tag{7}$$

where c_s is the speed of sound and w_i are standard weights defined for the specific DdQp lattice, and density and velocity are evaluated through Eqs. (2) and (3) [22]. After a rescaling $\delta x \equiv \delta t \equiv 1$, Eq. (5), considering Eq. (6), is discretized as follows:

$$f_i(\mathbf{x} + \mathbf{c}_i, t + 1) = f_i(\mathbf{x}, t) - \frac{1}{\tau} \left[f_i(\mathbf{x}, t) - f_i^{(eq)} \right]. \tag{8}$$

Eq. (8) is implemented in two steps: A local, non-linear *collision*:

$$\Xi_i(\mathbf{x}, t) = f_i(\mathbf{x}, t) - \frac{1}{\tau} \left[f_i(\mathbf{x}, t) - f_i^{(eq)} \right], \tag{9}$$

and a linear, non-local *streaming*:

$$f_i(\mathbf{x} + \mathbf{c}_i, t + 1) = \Xi_i(\mathbf{x}, t). \tag{10}$$

It is possible to demonstrate that, in the limit Ma $\ll 1$, Eq. (8) reproduces the incompressible Navier–Stokes equations [22], with pressure and kinematic viscosity defined as:

$$p := \rho c_s^2, \qquad \nu := c_s^2 \left(\tau - \frac{1}{2} \right). \tag{11}$$

The simple structure of the collision-streaming mechanism (Eqs. (9) and (10)) separates the non-linear from the non-local part; in particular, advection is linear and exact. In this way, the solution procedure does not require repeating iterations with residual check, thus allowing a very reduced number of operations per time update, and hence an unparalleled numerical efficiency.

2.2.2. Homogenised Lattice-Boltzmann model (HLBM)

In HLBM, both the continuous and particulate phase are described by a single particle distribution function $f_i(\mathbf{x}, t)$ obeying the Lattice-Boltzmann equation with a Bhatnagar–Gross–Krook (BGK) collision operator (Eq. (8)). A standard D3Q27 scheme [22] was used. The zeroth momentum ρ^C and the first momentum $\rho^C \mathbf{u}^C$ of f_i give the liquid phase density and velocity respectively, and are calculated via:

$$\rho^C(\mathbf{x}, t) = \sum_i f_i(\mathbf{x}, t), \tag{12}$$

$$\rho^C(\mathbf{x}, t) \mathbf{u}^C(\mathbf{x}, t) = \sum_i f_i(\mathbf{x}, t) \mathbf{c}_i. \tag{13}$$

The multiphase behaviour of the model is determined by the "lattice porosity" field $d(\mathbf{x}, t) \in [0, 1]$ following [35]. The equilibrium function is built as in the standard BGK model (Eq. (7)), but the first-momentum velocity $\mathbf{u}^C$ is replaced with $\mathbf{u}$:

$$f_i^{(eq)} = w_i \rho^C \left[1 + \frac{\mathbf{u} \cdot \mathbf{c}_i}{c_s^2} + \frac{(\mathbf{u} \cdot \mathbf{c}_i)^2 - c_s^2 u^2}{2c_s^4} \right], \tag{14}$$

where c_s is the speed of sound and w_i is the standard i-th weight for BGK D3Q27 models [22]. $\mathbf{u}$ is a linear combination of the particulate phase velocity $\mathbf{u}^P$ (to be discussed below, in Section 2.2.3) and the liquid phase velocity:

$$\mathbf{u} = \mathbf{u}^C(1 - d) + \mathbf{u}^P d. \tag{15}$$

The model reduces to [35] when $\mathbf{u}^P = \mathbf{0}$.

Depending on the local value of d, it is possible to identify three distinct areas: (*i*) $d = 0$ for continuous phase, which follows a standard BGK dynamics; (*ii*) $d = 1$ for nodes inside a particle, the treatment of which is described below in Section 2.2.3; and (*iii*) $0 < d < 1$ for intermediate nodes at the boundary of the particles (see again Section 2.2.3).

2.2.3. Particle representation in HLBM

For the sake of generality in describing the model, a "bubble" is herein indicated more generally as "particle". Each (spherical) particle $\mathscr{P}_K$ present inside the computational domain at a given time is formally represented as a tuple composed of centre-of-mass coordinate $\mathbf{X}_K$, velocity $\mathbf{U}_K$ and acceleration $\mathbf{a}_K$, angular coordinate ϑ_K, velocity $\mathbf{\Omega}_K$ and acceleration $\boldsymbol{\alpha}_K$, a radius R_K, a mass M_K, a moment of inertia $J_K \equiv 2/5 M_K R_K^2$ (for a sphere, referred to its centre of mass), and a smoothing parameter ε_K:

$$\mathscr{P}_K \equiv (\mathbf{X}_K, \mathbf{U}_K, \mathbf{a}_K, \vartheta_K, \mathbf{\Omega}_K, \boldsymbol{\alpha}_K, R_K, M_K, J_K, \varepsilon_K). \tag{16}$$

Through the smoothing parameter ε_K, an intermediate-porosity area with $0 < d < 1$ is defined on the border of the particle, at a distance from $\mathbf{X}_K$ comprised between $R_K - \varepsilon_K/2$ and $R_K + \varepsilon_K/2$. The porosity is defined in a way that allows it to vary continually and monotonically from 0 to 1 through a squared cosine function. This smooth-border solution has been shown to improve stability and reduce non-physical pressure and velocity fluctuations near the particle surface [20].

The hydrodynamic force $\mathbf{F}_K$ and torque $\mathbf{\Gamma}_K$ acting on the particle are computed from an algorithm similar to the one proposed by Ladd [23,24] to compute momentum exchange between bounceback nodes. The momentum exchanged between a node $\mathbf{x}$ and a contiguous node $\mathbf{x} + \mathbf{c}_i$ is:

$$g_i(\mathbf{x}) = \mathbf{c}_i[f_i(\mathbf{x}) - f_{\bar{i}}(\mathbf{x} + \mathbf{c}_i)], \tag{17}$$

where $\bar{i}$ is the opposite lattice direction of i. Then, force and torque are computed as follows:

$$\mathbf{F}_K = \sum_{\mathbf{x} \in \mathscr{P}_K} \sum_i g_i(\mathbf{x}), \tag{18}$$

$$\mathbf{\Gamma}_K = \sum_{\mathbf{x} \in \mathscr{P}_K} (\mathbf{x} - \mathbf{X}_K) \wedge \sum_i g_i(\mathbf{x}), \tag{19}$$

where "$\mathbf{x} \in \mathscr{P}_K$" means that all the nodes $\mathbf{x}$ such that $|\mathbf{x} - \mathbf{X}_K| \leq R_K + \varepsilon_K/2$ are included in the sum. The use of the abstract concept of the tuple in Eq. (16) to indicate $\mathscr{P}$, which limited the sums above only to the nodes effectively occupied by the particle, together with Newton's third law, ensure that the only non-null contributions from Eq. (17) come from the particle's surface nodes. In this way, surface-tracking procedures to force the sums in Eqs. (18) and (19) to be limited to only the particle's surface, as in Ladd [23,24], are avoided.

The particle's trajectory is updated at each timestep by solving second Newton's law of motion:

$$M_K \left(\frac{d\mathbf{U}_K}{dt} - \mathbf{g} \right) = \mathbf{F}_K, \tag{20}$$

$$J_K \frac{d\mathbf{\Omega}_K}{dt} = \mathbf{\Gamma}_K, \tag{21}$$

where $\mathbf{U}_K$ and $\mathbf{\Omega}_K$ are the centre-of-mass velocity and angular velocity respectively, and $\mathbf{g}$ is the acceleration due to gravity.

Eqs. (20) and (21) are solved through a leapfrog algorithm for linear variables:

$$\mathbf{a}_K(t + \Delta t) = \frac{1}{M_K}\mathbf{F}_K + \mathbf{g} \, ,$$

$$\mathbf{X}_K(t + \Delta t) = \mathbf{X}_K(t) + \mathbf{U}_K(t)\Delta T + \frac{1}{2}\mathbf{a}_K(t)\Delta t^2 \, , \qquad (22)$$

$$\mathbf{U}_K(t + \Delta t) = \mathbf{U}_K(t) + \frac{1}{2}[\mathbf{a}_K(t) + \mathbf{a}_K(t + \Delta t)]\Delta t \, ;$$

and angular:

$$\boldsymbol{\alpha}_K(t + \Delta t) = \frac{1}{J_K}\boldsymbol{\Gamma}_K \, ,$$

$$\vartheta_K(t + \Delta t) = \vartheta_K(t) + \boldsymbol{\Omega}_K(t)\Delta T + \frac{1}{2}\boldsymbol{\alpha}_K(t)\Delta t^2 \, , \qquad (23)$$

$$\boldsymbol{\Omega}_K(t + \Delta t) = \boldsymbol{\Omega}_K(t) + \frac{1}{2}[\boldsymbol{\alpha}_K(t) + \boldsymbol{\alpha}_K(t + \Delta t)]\Delta t \, .$$

Finally, for each lattice node $\mathbf{x} \in \mathscr{P}_K$, the particulate phase velocity $\mathbf{u}^P$ is updated:

$$\mathbf{u}^P(\mathbf{x}) = \mathbf{U}_K + \boldsymbol{\Omega}_K \wedge (\mathbf{x} - \mathbf{X}_K) \, . \qquad (24)$$

The effect of the HLBM procedure is to alter the equilibrium particle density functions defined on the lattice nodes. Therefore, only the usual LB stability criteria, as reported in Krüger et al. [22], apply. Throughout the numerical work described within this paper, no stability issue was encountered.

2.2.4. HLBM algorithm

The algorithm to update a timestep is divided into two sections: firstly, the system scrolls through all the particles, and for each it performs the following operations:

1. Force, $\mathbf{F}_K$, and torque, $\boldsymbol{\Gamma}_K$, are computed through Eqs. (17)–(19);
2. Centre-of-mass velocity $\mathbf{U}_K$ and angular velocity $\boldsymbol{\Omega}_K$ are computed through a Verlet algorithm (Eqs. (20) and (21)), and the centre of mass position $\mathbf{X}_K$ is updated;
3. For every node $\mathbf{x} \in \mathscr{P}_K$, $d(\mathbf{x})$ is updated based on the values of $\mathbf{X}$, R_K and ε_K;
4. For every node $\mathbf{x} \in \mathscr{P}_K$, $\mathbf{u}^P(\mathbf{x})$ is updated following Eq. (24).

The second section consists of a standard collision-streaming algorithm performed throughout the whole computational domain, following Eq. (8), considering Eqs. (14) and (15). On completion, the field d is reset in the whole domain.

2.2.5. Power-law model and turbulence

In non-Newtonian modelling, the equations of flow are resolved in the usual way (i.e., Newtonian), with the viscosity being altered pointwise through a given rheological model. As rheological models are built in such a way that the apparent rheology depends on the local shear rate, implementations of non-Newtonian models usually take the following shape: (*i*) the shear rate is computed locally in the usual way; (*ii*) the apparent viscosity is updated locally according to the given rheological model; (*iii*) the equations of motion are solved in the usual way. The Lattice-Boltzmann power-law model used in the work reported here [6] does not differ from this framework—the only peculiarity, being a Lattice-Boltzmann model, is that the relaxation time is altered through the rheological model, rather than the apparent viscosity directly, as the latter depends on the former. In addition, the implementation of the Smagorinsky turbulence model means that the relaxation time, once altered through the non-Newtonian model, is altered once again through the turbulence model. The combined power-law and Smagorinsky models are implemented in this work as follows.

Shear rate. It is well-known [22] that for any non-forced Lattice-Boltzmann model, the second momentum of the non-equilibrium term of the particle distribution function $f_i^{(1)}$ is related to the rate of shear tensor $\mathbf{S}$:

$$\mathbf{S} = -\frac{1}{2\tau \rho^C c_s^2}\sum_i f_i^{(1)} \mathbf{c}_i \otimes \mathbf{c}_i, \qquad (25)$$

where $\mathbf{S}$ is defined as:

$$S_{\alpha\beta} \equiv \frac{1}{2}\left(\partial_\alpha u_\beta^C + \partial_\beta u_\alpha^C\right) \qquad (26)$$

and, in turn:

$$\dot{\gamma} \equiv \sqrt{2\mathbf{S} : \mathbf{S}}. \qquad (27)$$

At every timestep, before the collision step, $\mathbf{S}(\mathbf{x})$ is evaluated locally through Eq. (25), and then $\dot{\gamma}(\mathbf{x})$ is computed through Eq. (27).

Power-law relaxation time. The dynamic viscosity $\mu(\mathbf{x})$ is evaluated through the power-law Eq. (1), and the relaxation time $\tau(\mathbf{x})$ is updated via the kinematic viscosity−relaxation time relationship [22]:

$$\nu \equiv \frac{\mu}{\rho^C} = c_s^2(2\tau - 1) \, . \qquad (28)$$

Combined power-law-Smagorinsky relaxation time. In order to take the possible effect of turbulence into account, a Smagorinsky term to the relaxation time is applied following Hou et al. [15]. $\mathbf{S}$ and $\dot{\gamma}$ are recomputed immediately after the power-law updating following Eqs. (25) and (27), then the (power-law) kinematic viscosity ν is substituted with the turbulent kinematic viscosity ν^{eff}:

$$\nu_{\text{eff}} = \nu + C_{\text{Smago}}\dot{\gamma} \, , \qquad (29)$$

where C_{Smago} is the Smagorinsky constant. In the work presented here, C_{Smago} was set to 0.14. Finally, the relaxation time τ comparing in the Lattice-Boltzmann Eq. (8) is substituted with the turbulent relaxation time τ_{eff}, which is computed from ν_{eff} following the same procedure in Eq. (28).

2.2.6. Partial-slip boundary condition

The partial-slip boundary condition described in Section 2.1.3 was implemented for flat surfaces in Lattice-Boltzmann as a hybrid bounce-back/free-slip, following Sbragaglia and Succi [31] and Benzi[3]. This boundary condition consists of a linear combination of half-way bounce-back [22] and free-slip [22]. If $f_i^\star(\mathbf{x}_B, t)$ is the particle distribution function after the collision step (i.e. the result of the computation at the right term of Eq. (8)) at a boundary node $\mathbf{x}_B$, then the streaming is altered as follows:

$$f(\mathbf{x}_B + \mathbf{c}_i, t + 1) = (1 - \xi)f_{\bar{i}}^\star(\mathbf{x}_B, t) + \xi f_{\tilde{i}}^\star(\mathbf{x}_B, t) \, , \qquad (30)$$

where $\xi \in [0, 1]$. $\bar{i}$ is the opposite lattice direction of i, and $\tilde{i}$ is the reflected direction of i, relative to the plane locally tangent to the boundary border. $\tilde{i}$ is set to $\bar{i}$ when it is not possible to find a valid reflected lattice direction for every i. However, the D3Q27 scheme ensures that every i has a valid reflected lattice direction.

The boundary condition expressed in Eq. (30) reduces to full bounce-back for $\xi = 0$, and to full free-slip for $\xi = 1$.

2.3. Experimental work

The experimental data used in the work reported here were produced by Dapelo et al. [10] and Sindall et al. [34]. Below, a description of the experimental rig and the visualization techniques is reported.
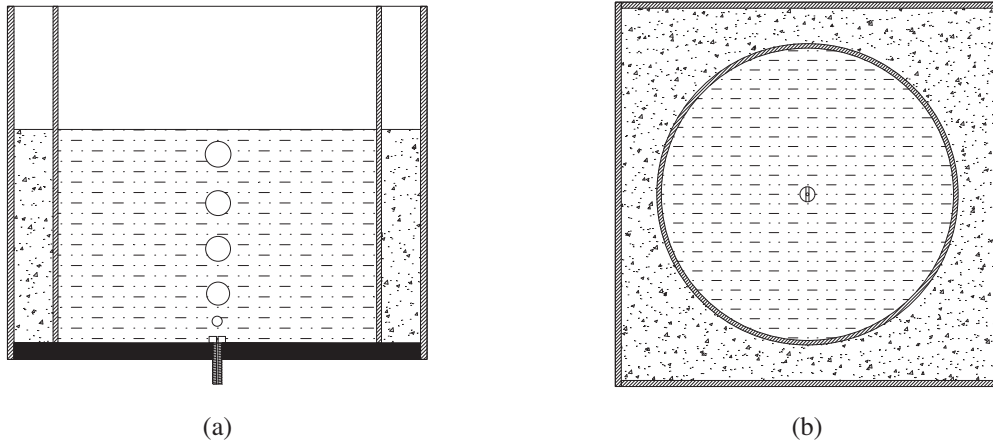
(a)

(b)

Fig. 1. Experimental rig: (a) top and (b) front view. Pump, flowmeter, pipes and fittings not shown. From Dapelo et al. [10].

Table 2
Power-law coefficients for CMC solutions, from Dapelo et al. [10].

Label (−)	Concentration (g ℓ^{-1})	K (Pa s^n)	n (−)
cmc02	2	0.054	0.805
cmc04	4	0.209	0.730

2.3.1. Transparent sludge substitute

As biokinetics was not considered in the work reported here, the common approach of substituting sludge with a transparent sludge substitute was followed Wu and Chen [44]. This allowed a simpler experimental rig to be built and enabled laser visualization data collection.

Sigma-Aldrich 419338 sodium carboxymetyl cellulose (CMC) with average molar weight of 700,000 was employed to prepare two water solutions, namely 2 and 4 g ℓ^{-1}, labelled as "cmc02" and "cmc04" respectively. The viscosity of the two solutions was measured in the shear rate interval 100−500 s^{-1} and fitted against the power-law Eq. (1). The results are reported in Table 2.

The two CMC solutions have rheological characteristics that are intermediate between 2.5 and 5.4% TS sludge (see Table 1).

2.3.2. Experimental rig

The experimental rig consisted of a 4 l cylindrical, transparent tank 20 cm diameter, filled to a depth of 13 cm with CMC (Fig. 1). An external transparent cubic vessel was filled with water in order to diminish the refraction of incident laser beams. Air was injected from the central nozzle at a flow rate of $q = 5.30$ ml s^{-1}.

The bubble plume was observed using a high-speed camera [10]. In both CMC concentrations, the plume was composed of equally-sized, equally-distributed bubbles rising at constant velocity. No bubble coalescence of breakup was observed. Bubble diameter and rising velocities were 7.01 mm and 0.48 m/s respectively for the "cmc02" solution, and 7.94 mm and 0.36 m/s for the "cmc04". In both cases, a deformation of the surface was observed (Fig. 2).

The particle Reynolds number is defined from the bubble diameter, its rising velocity and an average viscosity value:

$$\text{Re} \equiv \frac{2RU}{\langle \nu \rangle} . \tag{31}$$

The average viscosity $\langle \nu \rangle$ depends on the average shear rate $\langle \dot{\gamma} \rangle$ through Eq. (1). As shown below in Section 3.2, the flow patterns are characterized by a central zone, where liquid is set in
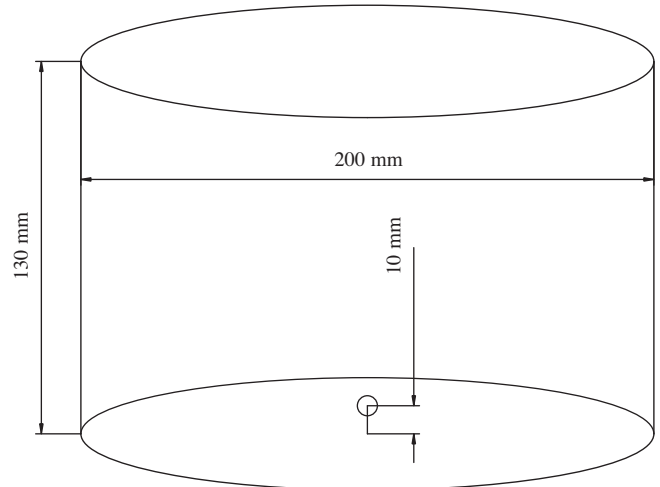

Fig. 2. Deformation of the surface, from Dapelo et al. [10].

Fig. 3. Computational domain.

motion by the rising bubble column and move upwards with approximately the same velocity of the bubbles on one side, and surrounding areas where velocity magnitude is around one order of magnitude lower. Hence, a good approximation for the average shear rate reads $\langle \dot{\gamma} \rangle \approx (U - 0)/R$ and Eq. (31) becomes:

$$\text{Re} = \frac{2RU}{K}\left(\frac{U}{R}\right)^{1-n} . \tag{32}$$

According to the Equation above, the Reynolds number assumes the values of 160 for "cmc02" and 47 for "cmc04".

2.3.3. Visualization techniques

Particle Image Velocimetry (PIV) and Positron Emission Particle Tracking (PEPT) were used to produce experimental data. The PIV
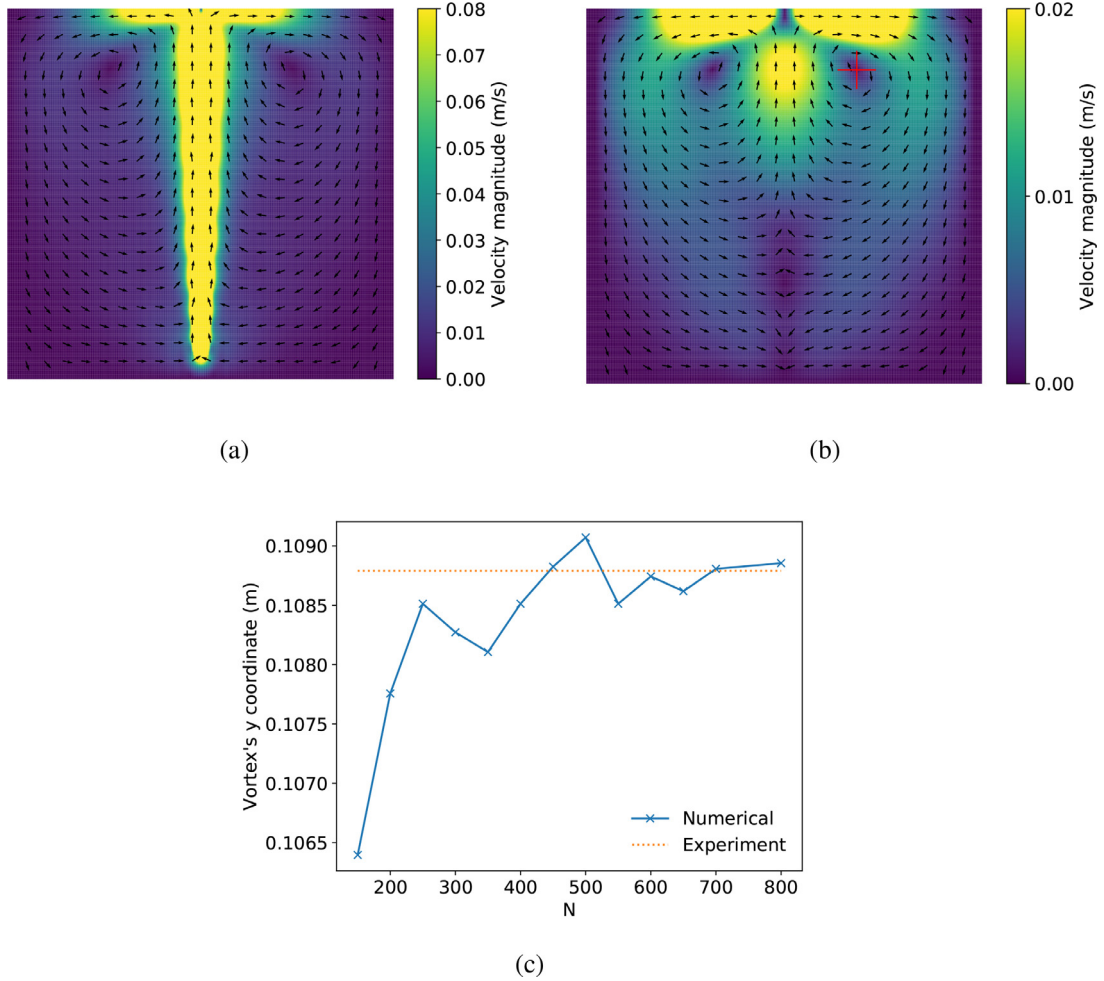
(a)

(b)

(c)

Fig. 4. Flow patterns and vortex's position in the PIV plane for "cmc04" simulation. (a) Flow patterns for $N = 400$, central plane. (b) Flow patterns for $N = 400$, PIV plane and with the vortex evident. (c) Vortex's y coordinate over linear grid size, compared to the experimental value (horizontal line).

setup is described in Dapelo et al. [10]. An incident laser beam produced a vertical plane 3 cm away from the cylinder's central axis (fhereafter referred to as the "PIV plane"), and tracked the liquid phase velocity projection over it. The cell size for the measurements was 64×64 pixels. Once the regime conditions for the flow and the bubbly motion had been reached, the average field was measured for a time of approximately 3 s.

The PEPT setup is described in Sindall et al. [34]. A 400 μm neutrally-buoyant tracer particle soaked with a γ-ray decaying aqueous solution and coated with an impermeable resin was injected into the CMC solution in the rig. An array of photomultipliers and scintillators tracked its trajectory for up to 40 min with a resolution of 0.6 mm. The information on the tracer particle's trajectory was then used to reconstruct the water phase's velocity field across a radial plane.

3. Results

The model discussed in Section 2.2 was validated against the data from experimental work described in Section 2.3. A test case reproduced geometrical data rheology described in Section 2.3. A zero-velocity Bouzidi boundary condition [5] was applied at the bottom and the lateral walls of the cylinder, and the partial-slip at the top. A circular crown at the most external part of the top surface, three cells thick, was set a zero-velocity Bouzidi boundary condition instead of the partial-slip to improve stability. The rest of the top surface was set to the partial-slip condition. The dimen-

sionless lattice velocity was set to 0.3 and the smoothing parameter ε_K to 1.2 for all the particles. Liquid phase and bubble density were set to 1000 and 1 kg m^{-3} respectively. The power-law parameters reported in Table 2 were adopted. Grids with a number N of lattice nodes across the diameter varying from 150 to 800 were considered. At the initial timestep, no bubble was present in the system, and the liquid phase velocity field was set to zero. A bubble was introduced (i.e., a new tuple $\mathscr{P}_K$ was defined) with the centre-of-mass $\mathbf{X}_K$ located at 1 cm above the bottom of the computational domain, along the central axis, every Δt_{inj} seconds, with Δt_{inj} being defined to match the flow rate q with the experimental values of the bubble diameters reported in Section 2.3.2:

$$\Delta t_{\mathrm{inj}} = \frac{4\pi R_K^3}{3\,q}\,. \tag{33}$$

A bubble was removed (i.e., the corresponding tuple $\mathscr{P}_K$ was undefined) when it touched the top surface of the computational domain. In Fig. 3, a schematic representation of the computational domain is given.

The numerical work was performed on up to eight 16-core (32-thread) Intel Xeon E5-2695 v4 "Broadwell" (2.20 GHz clock, 8 GT/s QPI bus) processors. For the number of nodes per diameter $N = 400$, the computational domain resulted to be 27,579,306 node large. The numerical expense was quantified as around 2.6×10^{-6} CPU second per thread per timestep per node (or cell in finite-volume CFD jargon). As a comparison, the numerical expense of a similar Euler–Lagrange, finite-volume CFD work on a domain of
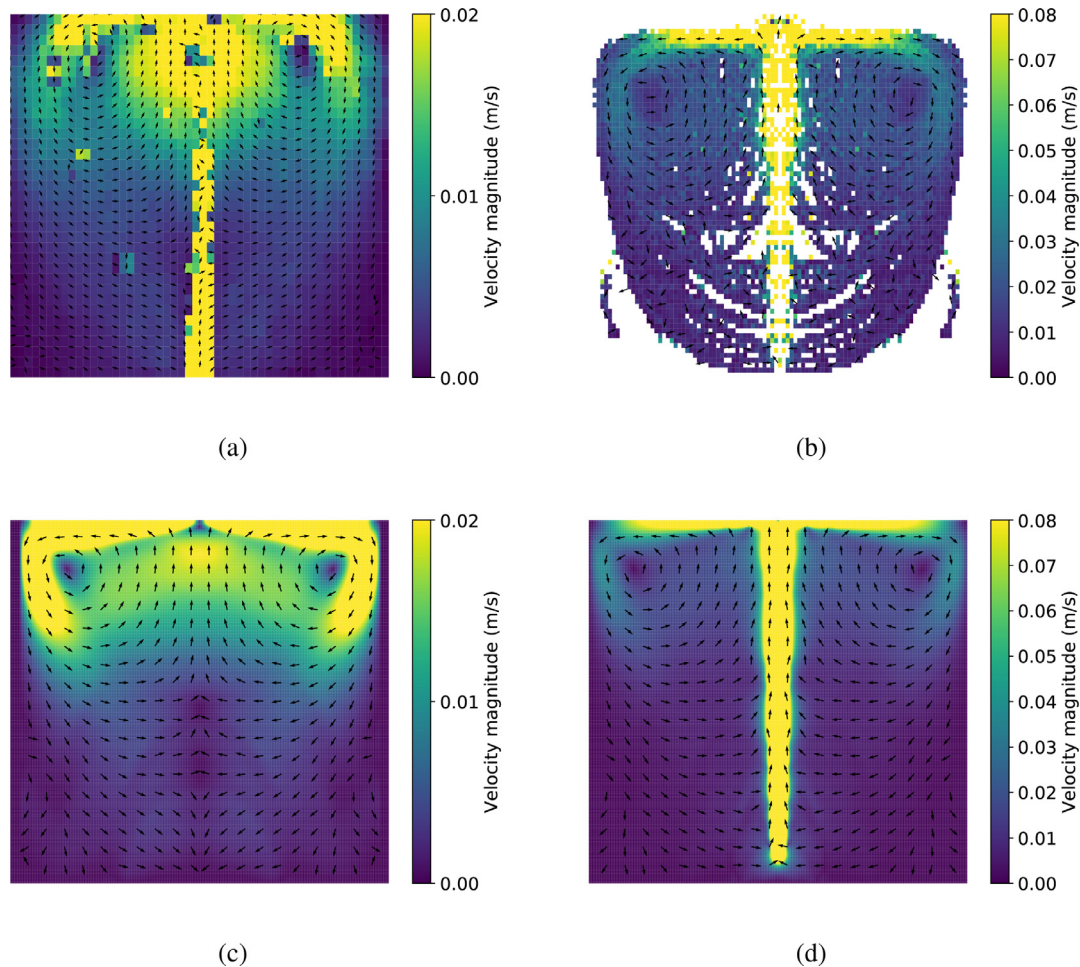
Fig. 5. Averaged flow patterns, "cmc02" runs, $\xi = 1$. (a) PIV experimental data, PIV plane. (b) PEPT experimental data, central plane. (c) Numerical data, PIV plane. (d) Numerical data, central plane.

1,361,367 cells [10], performed on three 8-core (16-thread) Intel Xeon E5-2660 "Sandy Bridge" (2.10 GHz clock, 9.6 GT/s QPI bus) processors, amounted to around 4.8×10^{-4} CPU second per thread per timestep per cell (or node in Lattice-Boltzmann jargon), around 180 times longer. Of course, a rigorous comparison of the two runs is not possible as they were performed on two different facilities with different hardware, and consequently, the datum of "180 times faster" should be read very carefully. Despite that, we consider that the advantage of the model presented in this paper over Dapelo et al. [10] is evident.

3.1. Mesh convergence

To evaluate mesh convergence, a series of runs corresponding to the "cmc04" solution were performed under acoustic scaling (i.e., lattice distance was varied while keeping lattice velocity constant) by varying N from 150 to 800. ξ was set to 1 (i.e., free-slip).

The resulting flow patterns are shown in Fig. 4(a) and (b). In all the numerical runs, axial symmetry was observed. The fluid phase is arranged in a fast-rising column in the proximity of the bubble plume. Once approaching the surface, the liquid phase is displaced towards the walls and then forms a toroidal vortex which brings fluid downwards and back towards the central column.

The position of the vortex (shown in Fig. 4(b)) was tracked, and the corresponding y coordinate plotted against N (Fig. 4(c)). The experimental value is reported for comparison. The relative deviation from experimental value resulted to be $\lesssim 2\%$ for all the runs,

and fell below 0.26% from $N = 400$ onwards. Hence, $N = 400$ was chosen for all the following numerical work as a balance between accuracy and computational expense. The error associated with numerical data produced from this grid can be considered to be the above-mentioned deviation of the numerical vortex position from the experimental value – that is, 0.26%.

3.2. Validation

In Fig. 5, a comparison between experimental and simulated flow patterns for the "cmc02" solution and $\xi = 1$, is shown.

As hypothesized in Dapelo et al. [10] and confirmed in Sindall et al. [34], the high-velocity central column which is present in Fig. 5(a) but absent in Fig. 5(c), is in fact an optical artefact affecting the PIV measurements and caused by refraction of the laser beam across the air bubbles. Considering this, the figure shows a good qualitative match between experimental and numerical flow patterns.

The most significant discrepancy between simulated and experimental flow patterns consists of an overestimation of the flow patterns intensity immediately below the surface, resulting in a horizontal displacement of the vortex towards the walls. Similar behaviour was also observed in the "cmc04" runs. In Section 2.1.3 it was hypothesized that this difference was likely to be due to the dissipative effect of the surface evolution on the bulk flow, which could not be captured by the simulations reported here. To prove this, another series of "cmc04" runs was performed. The resolution
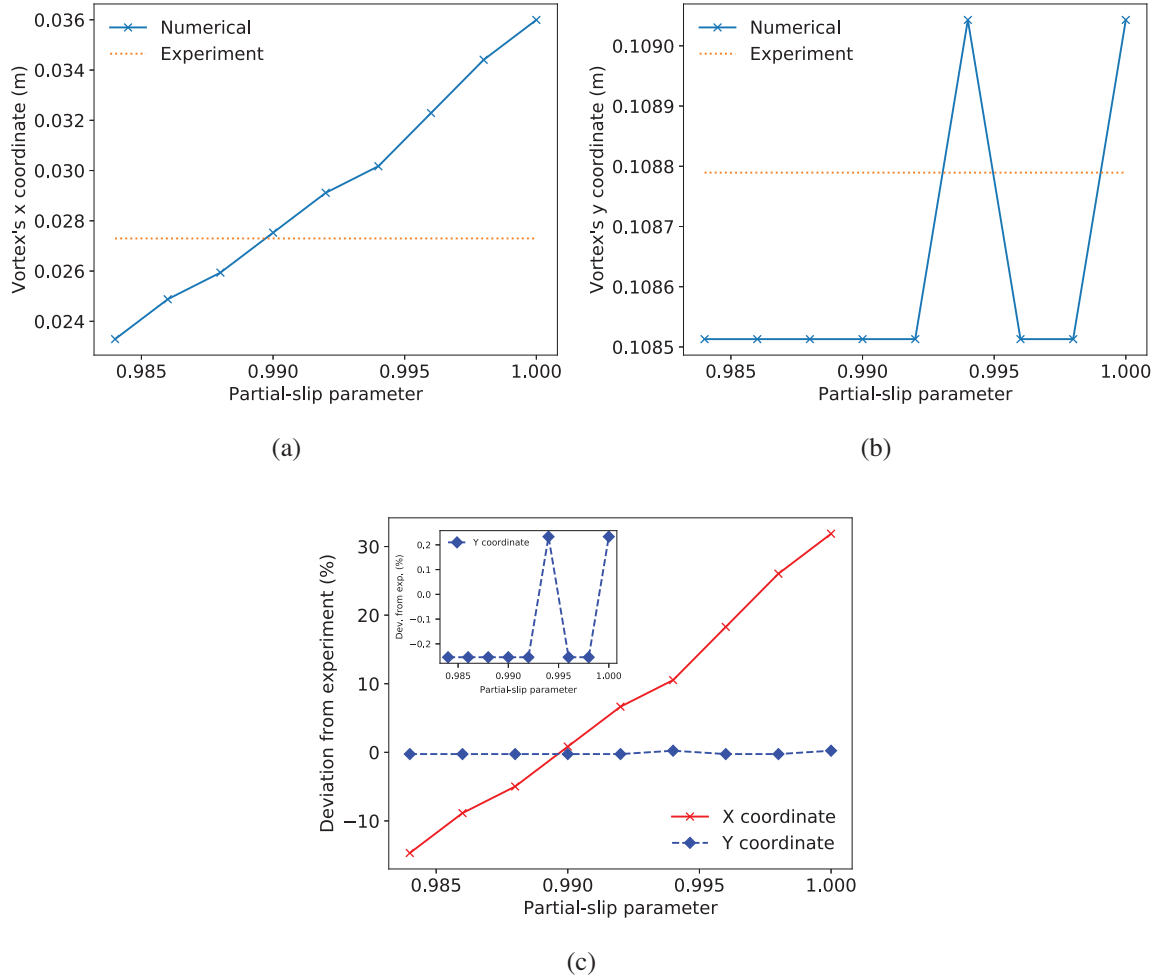
(a)

(b)

(c)

Fig. 6. Vortex's position over partial-slip parameter. (a) x and (b) y coordinates (solid lines) compared to experimental PIV data (pointed lines). (c) Percentage deviation from experimental data.

N was set to 400 nodes per diameter, and the partial-slip parameter ξ varied between 0.984 to 1. The position of the vortex was tracked and is shown in Fig. 6.

The vortex's y coordinate differed from the experimental value of 0.2% or less in all the cases. The x coordinate was shown to drop with the decreasing of ξ, and eventually matched the experimental value for $\xi \simeq 0.990$. This proves the effectiveness of the hybrid boundary condition in reproducing the surface dissipative effect. Even qualitatively, the improvement of the numerical prevision is evident, as shown in Fig. 7 for the "cmc02" runs.

4. Discussion

The Lattice-Boltzmann method offers a number of advantages over CFD. As reported in Section 3, the advantage of the Lattice-Boltzmann model described in this paper over an analogue Euler-Lagrange finite-volume CFD [10] was evident, despite the limitations of the comparison methodology. And this was achieved despite the Lattice-Boltzmann runs were performed over a number of processes more than five times larger than the CFD.

This performance improvement is due to two peculiarities of the collide-streaming mechanism (Eqs. (9) and (10)): (*i*) the direct time-advancing algorithm without iterations allows a considerably smaller number of operations per timestep per lattice node; and (*ii*) the locality of the collision step (Eq. (9)), together with the linearity of the streaming (Eq. (10)) makes sure that the inter-

processor communications are reduced to a minimum, thus facilitating multiprocessor scaling-up.

The increase of computational efficiency allows much finer grids for similar computational expenses: the overall computational expense of a typical run reported in this paper was around 2.6 times the expense of the Euler-Lagrange finite-volume CFD run in Dapelo et al. [10], but the number of lattice nodes was over twenty times larger. The increased level of mesh detail allowed the Lattice-Boltzmann work to resolve the bubbles as finite-dimensioned object rather than points, as in the above-mentioned CFD work. This latter approximation was a weakness of the CFD model, as it imposed constraints on the size of the cells which were expected to be crossed by the bubbles, and on the overall number of bubbles in the system at a given time. These constrains were obviously removed in the Lattice-Boltzmann model.

The Lattice-Boltzmann model imposes a cubic mesh with constant lattice size. Discretizations on unstructured or locally refined grids exist Krüger et al. [22]—at the cost, however, of partially compromising the simplicity and the parallelizability of the collide-streaming algorithm. However, the apparent limitation of a cubic mesh does not affect the results quality, because the increased resolution from a finer mesh widely counterbalances the staircase effect on the borders. Moreover, specific boundary conditions (e.g., Bouzidi) are specifically designed to remove the staircase effect. On the contrary, a simple cubic mesh allows to implement specific
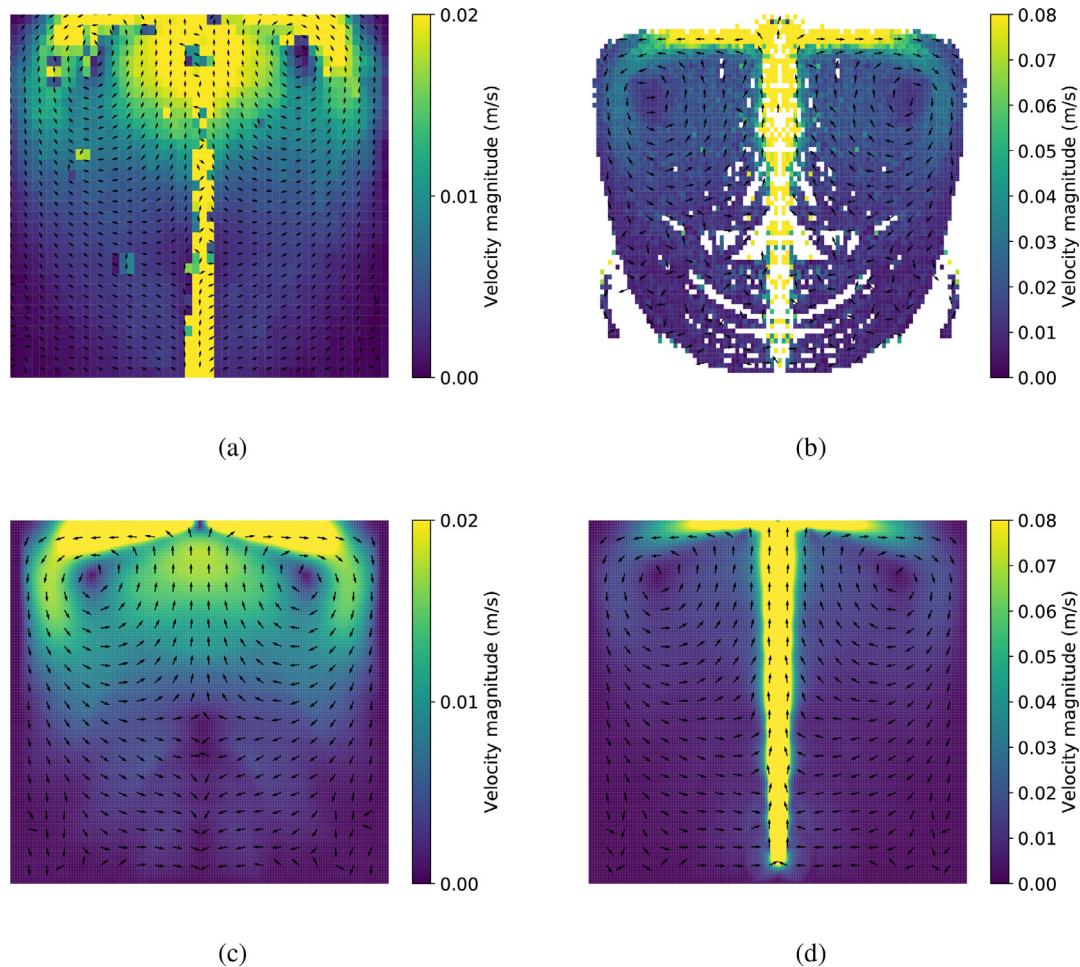
Fig. 7. Averaged flow patterns, "cmc02" runs, $\xi = 0.990$. (a) PIV experimental data, PIV plane. (b) PEPT experimental data, central plane. (c) Numerical data, PIV plane. (d) Numerical data, central plane.

modelling (in the work reported in this paper, HLBM) in a simple and natural way.

Finally, the way the Lattice-Boltzmann algorithm is defined in terms of lattice directions allows the formulation of a number of boundary conditions in a simple and natural way — notably, no-slip and free-slip in terms of bounce-back and reflection respectively, and partial-slip as a combination of the two. This constituted a furteher advantage over the CFD model, as offered the possibility to tune the surface dissipation, which was not possible in CFD.

5. Conclusions

A novel LB model for gas mixing in anaerobic digestion was proposed and validated against laboratory-scale data.

The model consisted of the combination of HLBM for multiphase modelling, a non-Newtonian model for liquid phase rheology, a Smagorinsky model for turbulence and a hybrid bounce-back/free-slip boundary condition for surface dissipation. The model was able to reproduce faithfully the experimental flow patterns.

The hybrid boundary condition was shown to reproduce the surface dissipative effect accurately.

The advantages of the Lattice-Boltzmann model over an Euler-Lagrange finite-volume CFD analogue and the increases numerical efficiency are described.

The innovative model will have applications in the modelling of complex flow patterns in laboratory, pilot and full scale anaerobic digesters, and represents a significant step forward in advancing the state of the art in this regard.

This work is the first step of a larger and ambitious project (see "Acknowledgements" below), in which biokinetics and hydrodynamics will be coupled and simulated together. Next steps will include a separated validation of a simplified biokinetic model, the validation of a coupled model against laboratory experimental data, and the application to full-scale digesters.

Declarations of interest

None.

Acknowledgements

References

[1] Achkari-Begdouri A, Goodrich PR. Rheological properties of moroccan dairy cattle manure. Bioresour Technol 1992;40:225–33. doi:10.1016/0960-8524(92)90201-8.

[2] Andersson B, Andersson R, Håkansson L, Mortensen M, Defence N, Sudiyo R, et al. Computational fluid dynamics for engineers. Cambridge University Press; 2012. ISBN 9781139093590.

[3] Benzi R, Biferale L, Sbragaglia M, Succi S, Toschi F. Mesoscopic modelling of heterogeneous boundary conditions for microchannel flows. J Fluid Mech 2006;548:257–80 arXiv:0502060. doi:10.1017/S0022112005007512.

[4] Bhatnagar PL, Gross EP, Krook M. A model for collision processes in gases. i. small amplitude processes in charged and neutral one-component systems. Phys Rev 1954;94(3):511–25. doi:10.1103/PhysRev.94.511.

[5] Bouzidi M, Firdaouss M, Lallemand P. Momentum transfer of a Boltzmann-lattice fluid with boundaries. Phys Fluids 2001;13:3452–9.

[6] Boyd J, Buick J, Green S. A second-order accurate lattice Boltzmann non-Newtonian flow model. J Phys A Math Gen 2006;39(46):14241–7. doi:10.1088/0305-4470/39/46/001.

[7] Bridgeman J. Computational fluid dynamics modelling of sewage sludge mixing in an anaerobic digester. Adv Eng Software 2012;44(1):54–62. doi:10.1016/j.advengsoft.2011.05.037.

[8] Council of the European Union. Council Directive of 21 May 1991 concerning urban waste water treatment (91/271/EEC). 1991. http://eur-lex.europa.eu/LexUriServ/LexUriServ.do?uri=CONSLEG:1991L0271:20081211:EN:PDF.

[9] Craig KJ, Nieuwoudt MN, Niemand LJ. CFD Simulation of anaerobic digester with variable sewage sludge rheology. Water Res 2013;47(13):4485–97. doi:10.1016/j.watres.2013.05.011.

[10] Dapelo D, Alberini F, Bridgeman J. Euler-Lagrange CFD modelling of unconfined gas mixing in anaerobic digestion. Water Res 2015;85:497–511. doi:10.1016/j.watres.2015.08.042.

[11] Dapelo D, Bridgeman J. Assessment of mixing quality in full-scale, biogas-mixed anaerobic digestion using CFD. Bioresour Technol 2018;265(April):480–9. doi:10.1016/j.biortech.2018.06.036.

[12] Dapelo D, Bridgeman J. Euler-Lagrange computational fluid dynamics simulation of a full-scale unconfined anaerobic digester for wastewater sludge treatment. Adv Eng Softw 2018;117:153–69. doi:10.1016/j.advengsoft.2017.08.009.

[13] Eshtiaghi N, Markis F, Yap SD, Baudez JC, Slatter P. Rheological characterisation of municipal sludge: a review. Water Res 2013;47(15):5493–510. doi:10.1016/j.watres.2013.07.001.

[14] European Environment Agency. Waterbase - UWWTD: urban waste water treatment directive - reported data. Tech. Rep.; 2015. http://www.eea.europa.eu/data-and-maps/data/waterbase-uwwtd-urban-waste-water-treatment-directive-4.

[15] Hou S, Sterling J, Chen S, Doolen GD. A lattice Boltzmann subgrid model for high Reynolds number flows. In: Lawniczak: A, Kaprak R, editors Pattern formation and lattice gas automata, vol 6. AMS - Fields Institute Communications; 1996. ISBN 978-0-8218-0258-8 arXiv:9401004. http://books.google.com/books?hl=en&lr=&id=TIdy6-ItW7YC&oi=fnd&pg=PA151&dq=A+Lattice+Boltzmann+Subgrid+Model+for+High+Reynolds+Number+Flows&ots=zqrEqXjMNL&sig=_76MYxU-XPd2n1iKsPD5rIJQ7-Q

[16] Hreiz R, Adouani N, Fünfschilling D, Marchal P, Pons MN. Rheological characterization of raw and anaerobically digested cow slurry. Chem Eng Res Des 2017;119:47–57. doi:10.1016/j.cherd.2017.01.005.

[17] Hurtado F, Kaiser A, Zamora B. Fluid dynamic analysis of a continuous stirred tank reactor for technical optimization of wastewater digestion. Water Res 2015;71:282–93. doi:10.1016/j.watres.2014.11.053.

[18] Karim K, Thoma GJ, Al-Dahhan MH. Gas-lift digester configuration effects on mixing effectiveness. Water Res 2007;41(14):3051–60. doi:10.1016/j.watres.2007.03.042.

[19] Khan MAI, Delbosc N, Noakes CJ, Summers J. Real-time flow simulation of indoor environments using Lattice Boltzmann method. Build Simul 2015;8(4):405–14. doi:10.1007/s12273-015-0232-9.

[20] Krause MJ, Klemens F, Henn T, Trunk R, Nirschl H. Particle flow simulations with homogenised Lattice Boltzmann methods; 2017. p. 1–13. doi:10.1016/j.partic.2016.11.001. (In press)

[21] Kress P, Nägele HJ, Oechsner H, Ruile S. Effect of agitation time on nutrient distribution in full-scale CSTR biogas digesters. Bioresour Technol 2018;247(September 2017):1–6. doi:10.1016/j.biortech.2017.09.054.

[22] Krüger T, Kasumaatmaja H, Kuzmim A, Shardt O, Silva G, Viggen EM. The Lattice Boltzmann method. March 2015, Springer; 2017. ISBN 9783319446479. doi:10.1007/978-3-319-44649-3.

[23] Ladd AJC. Numerical simulations of particulate suspensions via a discretized Boltzmann equation. Part 1. Theoretical foundation. J Fluid Mech 1994;271:285–309.

[24] Ladd AJC. Numerical simulations of particulate suspensions via a discretized Boltzmann equation. Part 2. Numerical results. J Fluid Mech 1994;271:311–99.

[25] Landry H, Laguë C, Roberge M. Physical and rheological properties of manure products. Appl Eng Agric 2004;20(3):277–88. doi:10.13031/2013.16061.

[26] Lebranchu A, Delaunay S, Marchal P, Blanchard F, Pacaud S, Fick M, et al. Impact of shear stress and impeller design on the production of biogas in anaerobic digesters. Bioresour Technol 2017;245(June):1139–47. doi:10.1016/j.biortech.2017.07.113.

[27] Meister M, Rezavand M, Ebner C, Pümpel T, Rauch W. Mixing non-Newtonian flows in anaerobic digesters by impellers and pumped recirculation. Adv Eng Softw 2018;115(February 2017):194–203. doi:10.1016/j.advengsoft.2017.09.015.

[28] Meroney RN, Colorado PE. CFD Simulation of mechanical draft tube mixing in anaerobic digester tanks. Water Res 2009;43(4):1040–50. doi:10.1016/j.watres.2008.11.035.

[29] Owen WF. Anaerobic treatment processes. Energy in wastewater tall wreatment. Englewood Cliffs, NJ: Prentice-Hall, Inc.; 1982.

[30] Peskin CS. The immersed boundary method. Acta Numerica 2002;11:479–517. doi:10.1017/S0962492902000077.

[31] Sbragaglia M., Succi S. Analytical calculation of slip flow in lattice Boltzmann models with kinetic boundary conditions 2004;1–27. arXiv:0410039 doi:10.1063/1.2044829.

[32] Shan X, Chen H. Lattice Boltzmann model for simulating flows with multi phases and components. Physical Review E 1993;47(3):1815–19. doi:10.1103/PhysRevE.47.1815.

[33] Sindall RC, Bridgeman J, Carliell-Marquet C. Velocity gradient as a tool to characterise the link between mixing and biogas production in anaerobic waste digesters. Water Sci Technol 2013;67(12):2800–6. doi:10.2166/wst.2013.206.

[34] Sindall RC, Dapelo D, Leadbeater T, Bridgeman J. Positron emission particle tracking (PEPT): a novel approach to flow visualisation in lab-scale anaerobic digesters. Flow Meas Instrum 2017;54:250–64. doi:10.1016/j.flowmeasinst.2017.02.009.

[35] Spaid MAA, Phelan FR. Lattice Boltzmann methods for modeling microscale flow in fibrous porous media. Phys Fluids 1997;9(9):2468–74. doi:10.1063/1.869392.

[36] Swift M, Orlandini E, Osborn W, Yeomans J. Lattice Boltzmann simulations of liquid-gas and binary fluid systems. Phys Rev E 1996;54(5):5041–52. doi:10.1103/PhysRevE.54.5041.

[37] Swift MR, Osborn WR, Yeomans JM. Lattice Boltzmann simulation of nonideal fluids. Phys Rev Lett 1995;75(5):830–3.

[38] Terashima M, Goel R, Komatsu K, Yasui H, Takahashi H, Li YY, et al. CFD Simulation of mixing in anaerobic digesters. Bioresour Technol 2009;100(7):2228–33. doi:10.1016/j.biortech.2008.07.069.

[39] Trunk R, Marquardt J, Thäter G, Nirschl H, Krause MJ. Towards the simulation of arbitrarily shaped 3D particles using a homogenised lattice boltzmann method. Computers & Fluids 2018. doi:10.1016/j.compfluid.2018.02.027.

[40] Uhlmann M. An immersed boundary method with direct forcing for the simulation of particulate flows. J Comput Phys 2005. doi:10.1016/j.jcp.2005.03.017.

[41] Vesvikar MS, Al-Dahhan MH. Flow pattern visualization in a mimic anaerobic digester using CFD. Biotechnol Bioeng 2005;89(6):719–32. doi:10.1002/bit.20388.

[42] WaterUK. Sustainability Indicators 2010–2011. Tech. Rep. Water UK: London; 2012. http://water.wuk1.emsystem.co.uk/home/news/press-releases/indicators2010-11/water-uk---sustainability-report-2010-11.pdf%5Cnfiles/1080/WaterUK_2012_SustainabilityIndicators2010-2011.pdf.

[43] Wu B. CFD Simulation of gas and non-Newtonian fluid two-phase flow in anaerobic digesters. Water Res 2010;44(13):3861–74. doi:10.1016/j.watres.2010.04.043.

[44] Wu B, Chen S. CFD Simulation of non-Newtonian fluid flow in anaerobic digesters. Biotechnol Bioeng 2008;99(3):700–11. doi:10.1002/bit.21613.

[45] WWAP (World Water Assessment Programme). The United Nations World Water Development Report 4: Managing Water under Uncertainty and Risk. Tech. Rep. Paris: UNESCO; 2012. http://www.unesco.org/new/fileadmin/MULTIMEDIA/HQ/SC/pdf/WWDR4Volume1-ManagingWaterunderUncertaintyandRisk.pdf.

[46] Zhang Y, Yu G, Yu L, Siddhu MAH, Gao M, Abdeltawab AA, et al. Computational fluid dynamics study on mixing mode and power consumption in anaerobic mono- and co-digestion. Bioresour Technol 2016;203:166–72. doi:10.1016/j.biortech.2015.12.023.